CILAMCE 2017
Florianópolis - Santa Catarina - Brazil

SIMULATION OF A COLUMN COLLAPSE FOR DENSE GRANULAR FLOWS

Linda Gesenhues

linda@nacad.ufrj.br

José J. Camata

camata@nacad.ufrj.br

Alvaro L.G.A. Coutinho

alvaro@nacad.ufrj.br

High Performance Computing Center, Federal University of Rio de Janeiro

P.O. Box 68506, RJ 21945-970, Rio de Janeiro, Brazil

Abstract. *In many situations in science and engineering, it is necessary to study dense granular flows. More and more studies about the rheology and possible constitutive models of such flows are published. However, predicting those dense granular flows is still challenging. The viscoplastic flow behavior changes according to the particle concentration. Various constitutive rheology models can express this behavior. A model focusing on dense granular flow is the so-called* $\mu(I)$*-rheology. In this model, an empirical relation links the tangential stresses to normal ones. Therefore, the pressure has a direct influence on the viscosity. This model provides a non-conventional shear-thinning behavior, which is depending on the shear rate and local pressure. Due to the flow complexity and the high nonlinearity, difficulties often occur. Thus, regularization is needed, as well as, a careful choice of the simulation parameters. In this study, we take a closer look at the regularization and its influence on the results. A column collapse is simulated using the* $\mu(I)$*-rheology aiming to create guidelines for the regularization and other characteristics of this particular case. Experiments are done using a two-phase Navier-Stokes solver based on the variational multiscale method. The formulation is implemented in* `libMesh`*, considering adaptive mesh refinement. The results are discussed, and limitations of the model are shown.*

Keywords: $\mu(I)$*-rheology, dense granular flow, non-Newtonian flow, regularization, design of experiments*

1 INTRODUCTION

Dense granular flows occur in various industrial applications, as well as, in nature (Forterre & Pouliquen, 2008). Especially in geophysics, dense granular flow is present in rock avalanches, landslides and turbidity currents. Turbidity currents are underflows responsible for sediment deposits that build and transform geological formations in the deep sea. Predicting and understanding those geological changes is of high importance to the oil and gas industry, e.g., to determine an advantageous drilling location. Those decisions involve a high investment budget. Thus, numerical simulation is a useful predictive tool, contributing to diminishing risks and, consequently, saving time and costs. Turbidity currents like mud avalanches often involve dense granular flow. By exceeding a certain particle concentration in the fluid, the flow behavior turns non-Newtonian. This behavior is considered in the fluid simulation solver by a constitutive model.

The $\mu(I)$-rheology is a constitutive model for dense granular flow introduced by Pouliquen & Forterre (2002). Jop et al. (2006) extend it to a three-dimensional model. Even though the $\mu(I)$-rheology is an empirical model based on phenomena observed in experiments, it has its origin in friction behavior of particles. It combines Coulomb friction, which considers that tangential stresses are proportional to the normal ones, and an inertial number, relating the microscopic and macroscopic timescales of the particle rearrangement. Therefore, the pressure has a direct influence on the viscosity. From a rheological point of view, this model provides a non-conventional shear-thinning viscoplastic behavior, which depends on the strain rate and the local pressure.

Lagrée et al. (2011) compare continuous simulation using the $\mu(I)$-rheology to results of DEM simulation of granular collapse. Staron et al. (2013) compute the discharge of a granular silo investigating the parameters of the $\mu(I)$-rheology. Ionescu et al. (2015) model a column collapse utilizing the $\mu(I)$-rheology reformulating it in the framework of a Drucker-Prager plasticity. Riber et al. (2016) suggest numerical tools to handle dam-break simulations of granular materials. Although more and more studies about the $\mu(I)$-rheology are published, it remains a challenge to simulations. Due to the complexity and the high nonlinearity, often complications as oscillations and divergence occur. As a consequence, several tools are required to achieve a good solution.

A common difficulty is the wide range of viscosity values experienced by the fluid. As the fluid becomes solid, its viscosity tends to infinity. Therefore, the constitutive model has a high need for regularization. In the area of non-Newtonian fluids, regularization is a common way to overcome numerical difficulties associated with extreme parameter values. Examples of popular regularization strategies are the Papanstasiou (Papanastasiou, 1987) and Bercovier-Engelman regularization (Bercovier & Engelman, 1980). A review of this topic can be found in Mitsoulis (2007) and Frigaard & Nouar (2005). The choice of the regularization parameter is always a compromise between accuracy, compared to the ideal model, and convergence.

In general, the dependence of the viscosity on the strain rate and pressure adds nonlinearities to the governing equations. Thus, solving the transient and incompressible Navier-Stokes equations becomes more complicated. The convection term and equal order interpolation of the velocity and pressure fields can lead to instabilities of the Galerkin formulation and consequently result in divergence and oscillations. As a consequence, stabilization strategies are necessary to ensure convergence and stability of the solution.

A widely used stabilization technique is based on approximating the unresolved scales. The variational multiscale method (VMS) was first proposed in Hughes (1995). The VMS method decomposes field variables into coarse and subscale components. The coarse scale is computed numerically while the fine scale is approximated (Hughes, 1995; Hughes et al., 1998, 2004). In the last two decades, VMS became a favorite tool for many problems. Recent reviews can be found in Gravemeier (2003); Hughes et al. (2004); Ahmed et al. (2015); John (2006); Rasthofer & Gravemeier (2017). The subscales can be either determined based on the residuum (residual-based variational multiscale (RBVMS)), on projection (orthogonal subgrid scale (OSS)) or even by bubble enrichment. Masud & Kwack (2011) simulate incompressible shear-rate depending non-Newtonian fluids calculating the subscale using bubble functions. Moreno et al. (2016) and **?** model Bingham and Herschel-Bulkley flows applying the OSS method to the governing equations. Castillo & Codina (2014a) show examples of a three-field Navier-Stokes problem for Power Law and Carreau-Yosada fluids using RBVMS and OSS stabilization. Furthermore, RBVMS and OSS stabilization are analyzed for viscoelastic flows (Castillo & Codina, 2014b; Codina & Castillo, 2016). Riber et al. (2016) combine RBVMS with adaptive mesh refinement to compute high Reynolds, and Bingham number flows. Several approaches can be used to estimate the subscales. Examples can be found in Moreno & Cervera (2015), Moreno et al. (2016) and Riber et al. (2016).

Designing an appropriate and effective mesh plays a big role, considering the inherent difficulties of computing dense granular flows. Especially, to determine the unyielded regions in viscoplastic flows adaptive mesh refinement (AMR) is a helpful tool which is more and more applied. Roquet and Saramito do several studies using AMR for Bingham flows (Roquet et al., 2000; Saramito & Roquet, 2001; Roquet & Saramito, 2003). Syrakos et al. (2013) use a multigrid algorithm to solve viscoplastic flows for a wide range of Bingham numbers. Zhang (2010) presents an augmented Lagrangian approach to solve Bingham flows applying AMR based on the resulting regularity of the solution. Riber et al. (2016) apply anisotropic AMR with highly stretched elements. The column collapse is an important benchmark to validate and verify free surface flows. Since it is a common, widely used problem, which has been used by various authors, it provides a good possibility to introduce new methods and models.

In engineering, design of experiments (DOE) is a constructive instrument of statistical quality control. It can be utilized for optimization and system design. DOE methods include experimental planing and fitting a regression model of the modified inputs to the output (Allen, 2010). The $\mu(I)$-rheology is affected by many parameters. It is of interest to understand how varying the input parameters relates to the output responses. This can be analyzed by statistically planned numerical experiments and evaluated responses.

The objective of this study is to use the tools like regularization strategies, VMS and AMR to compute column collapse of dense granular flows. Here, we are taking a closer look at the regularization parameters of the applied $\mu(I)$-rheology and the surrounding Newtonian fluid by applying DOE, aiming to create guidelines for the regularization and other characteristics of interest. The paper is organized as follows: the applied methods can be found in Section 2, Section 2.2 contains a more detailed description of the $\mu(I)$-rheology, Section 2.3 outlines the regularization strategies used in this study, Section 3 presents the results of the DOE of the input variables and in Section 4 a conclusion is given with a discussion and outlook.

2 METHODS

2.1 Governing equations

On a spatial domain $\Omega \subset R^3$, with a piecewise regular surface and time interval $[0, t_f]$, an incompressible and viscous fluid is governed by the Navier-Stokes equations:

$$\rho\left(\frac{\partial \mathbf{u}}{\partial t} + \mathbf{u}\cdot\nabla\mathbf{u}\right) - \nabla\cdot\boldsymbol{\sigma} = \mathbf{f} \quad \text{on } \Omega\times(0,t_f)\,, \tag{1}$$

$$\boldsymbol{\nabla}\cdot\mathbf{u} = 0 \quad \text{on } \Omega\times(0,t_f)\,, \tag{2}$$

where $\mathbf{u}$ represents the velocity field, ρ is the fluid density, $\boldsymbol{\sigma}$ holds the stress tensor and $\mathbf{f}$ denotes the body force. The Dirichlet and natural boundary conditions are applied on the complementary subsets Γ_1 and Γ_2 of the boundary Γ:

$$\mathbf{u} = \mathbf{g} \quad \text{on } \Gamma_1\,, \tag{3}$$

$$\mathbf{n}\cdot\boldsymbol{\sigma} = \mathbf{h} \quad \text{on } \Gamma_2\,. \tag{4}$$

The stress tensor $\boldsymbol{\sigma}$ can be described by:

$$\boldsymbol{\sigma}(p,\mathbf{u}) = -p\mathbf{I} + \mathbf{T}\,, \tag{5}$$

where $\mathbf{I}$ is the identity tensor and p denotes the total pressure. For a Newtonian fluid, the relationship between the stress tensor $\boldsymbol{\sigma}$ and the strain rate $\dot{\boldsymbol{\gamma}}$ is linear. Thus, the dynamic viscosity η is constant. However, the viscosity of a dense granular fluid is dependent on other flow parameters such as the norm of the deformation rate and the pressure. So that the deviatoric part of the stress tensor $\mathbf{T}$ is stated as:

$$\mathbf{T} = 2\eta(\|\dot{\gamma}\|, p)\dot{\boldsymbol{\gamma}}\,, \tag{6}$$

here, η describes the dynamic viscosity and $\dot{\boldsymbol{\gamma}}$ holds the strain rate tensor, which is defined as:

$$\dot{\boldsymbol{\gamma}} = (\nabla\mathbf{u} + \nabla^T\mathbf{u})\,. \tag{7}$$

The norm of the strain rate tensor can be calculated by its second invariant:

$$\|\dot{\gamma}\| = \left(\frac{1}{2}\dot{\boldsymbol{\gamma}} : \dot{\boldsymbol{\gamma}}\right)^{0.5}\,. \tag{8}$$

2.2 The $\mu(I)$-rheology

The $\mu(I)$-rheology is based on the Coulomb friction, which assumes that the normal stress, which is applied by the pressure, is proportional to the tangential stress τ. So that $\tau = \mu p$, where μ is a friction coefficient. However, the $\mu(I)$-rheology relates the friction parameter to the flow by the inertial number I. This number is non-dimensional and represents the local state of the granular packing:

$$I = \frac{\|\dot{\gamma}\|d}{\sqrt{(p/\rho_g)}}\,, \tag{9}$$

where d is the grain diameter and ρ_g denotes the grain density. The inertial number I can be interpreted as a ratio of the macroscopic deformation timescale $(1/\|\dot{\gamma}\|)$ and the inertial timescale $\left(d^2\rho_g/p\right)^{0.5}$. Thus, the dynamic viscosity η is given by:

$$\eta = \frac{\mu(I)p}{\|\dot{\gamma}\|}\,. \tag{10}$$

Jop et al. (2005) propose a law for the friction coefficient based on experiments executed by Pouliquen & Forterre (2002) and Pouliquen (1999). The friction coefficient $\mu(I)$ starts from a critical value μ_s and converges towards a limiting value μ_2, so that:

$$\mu\left(I\right) = \mu_s + \frac{\mu_2 - \mu_s}{I_0/I + 1}\,, \tag{11}$$

here, I_0 is a constant. μ_s, μ_2 and I_0 are empirical determined by experiments.

2.3 Regularization

The complexity of the $\mu(I)$-rheology law requires several regularization steps. The need for regularization arises due to three causes: first, to fulfill mathematical continuity, which includes that none of the terms is divided by zero; second, due to physics, e.g., it is unphysical that the viscosity gets negative or zero; and last, regularization is also necessary to ensure the convergence of the solver as the fluid gets to a quasi-solid state.

Considering that the denominator of each term of the viscosity function cannot be equal to zero and reviewing Eqs. (9), (10) and (11), it follows that if the pressure p, strain rate norm $\|\dot{\gamma}\|$ and inertial number I get zero, the function does not deliver valid results. Frigaard & Nouar (2005) give an overview on how to use common regularization techniques in such cases. Chauchat & Médale (2014) summarize and apply them for the $\mu(I)$-rheology. In this study, we add a simple regularization parameter, which consists of a small number, to the denominators. This way we ensure that even though the pressure, strain rate norm or inertial number get zero, the denominator still holds a small number.

Moreover, considering Eq. (10), the viscosity gets zero when the pressure gets zero. A zero pressure can occur, e.g., due to the boundary condition. However, a zero viscosity is physically not possible and has to be avoided. Therefore, we set a minimum viscosity which serves as a lower limit.

On the contrary, for high pressure values, the viscosity of the fluid rises and is comparable with the viscosity of a solid. Consequently, our fluid solver has difficulties to converge. Thus, we impose a maximum viscosity, which limits the viscosity as it gets too high. As a result, the viscosity is bounded above and below, as:

$$\eta = min\{max\{\eta_{min},\, \eta\left(\|\dot{\gamma}\|,\, p\right)\}\,, \eta_{max}\}\,. \tag{12}$$

The choice of the minimum and maximum viscosity is a compromise between convergence and accuracy. Lagrée et al. (2011) and Staron et al. (2014) give some guidelines on how to choose the maximum and minimum viscosity. However, we experience in our tests a strong influence of these values, making it difficult to achieve general guidelines. Evaluating the effects of the maximum viscosity limit on the results is part of our study.

2.4 Volume-of-Fluid formulation

The simulation of a two-phase flow, like the dam break in Section 3, requires a method to track the interface between the fluids. One possibility is to use the Volume–of–Fluid (VOF) formulation. The VOF method needs a marking function $\phi(\mathbf{x}, t)$ on a spatial domain $\Omega \subset R^3$ and along a time interval $[0, t_f]$, which has a precise regular boundary Γ and a continuous velocity field $\mathbf{u} \equiv \mathbf{u}(\mathbf{x}, t)$. The marking function is governed by:

$$\frac{\partial \phi}{\partial t} + \mathbf{u} \cdot \nabla \phi = 0\,. \tag{13}$$

The heavy fluid is assigned, for example, to $\phi(\mathbf{x}, t) = 1$, whereas the light fluid refers to $\phi(\mathbf{x}, t) = 0$. The interface of the two fluids is described by fractions of the markers. We assume that the interface is at $\phi = 0.5$. Thus, physical properties like the fluid density ρ and the viscosity η can be determined as follows:

$$\rho = \phi \rho_H + (1 - \phi) \rho_L\,, \tag{14}$$

$$\eta = \phi \eta_H + (1 - \phi) \eta_L\,, \tag{15}$$

where the indexes H and L denote the heavy and the light fluid. For more information on how we implement the VOF method refer to Elias & Coutinho (2007).

Applying the VOF method on test cases which are already hardly converging holds some difficulties. Often the interface is not clear distributed but spreading over a wider area. So that a great area can be found where $0 < \phi < 1$. The VOF method assumes that the interface is at $\phi = 0.5$. The spreading of the interface leads to mass loss. To improve mass conservation we imply a tangent function to transform ϕ to F_ϕ. The tangent function contracts the spread area to a finer and more distinct interface. The tangent function is given by (Elias & Coutinho, 2007):

$$F_\phi = tan\left((1 - \epsilon)\, \pi\, (\phi - 0.5)\right)\,, \tag{16}$$

where we assume $\epsilon = 0.1$. Afterwards, the marker ϕ is recovered by an inverse function as follows:

$$\phi = \frac{arctan F_\phi}{(1 - \epsilon)\, \pi} + 0.5\,. \tag{17}$$

Another issue using the VOF formulation might be the transition from the light fluid to the heavy fluid at a no-slip boundary condition. Since the velocity, at such a boundary condition is zero, the nodes on the boundary keep the former marker value. Over time this phenomenon leads to a finger of one element thickness of the light fluid under the heavy fluid. Once the light fluid is under the heavy fluid it acts like a slip boundary condition and distorts the result. Thus, we implement a procedure that as the marker function on the node over the no-slip boundary node gets higher than 0.5 the boundary node receives the marker value of the node above.

Lastly, since we are studying the behavior of fluids with $\mu(I)$-rheology, the lighter fluid is of minor interest. However, the fluid characteristics of the light fluid have a major influence on the convergence and also on the flow behavior of the heavy fluid. Often air is assumed as light fluid, but the low viscosity usually leads to convergence issues. Therefore, a more viscous and denser fluid than air is computed. In this study, we observe the effects of the parameters, like viscosity and density, of the light fluid on the results.

2.5 Variational multiscale method

In the VMS approach, the unknowns are split into two scales: a coarse scale and a subscale. So that:

$$\mathbf{u} = \mathbf{u}^h + \mathbf{u}' \,, \tag{18}$$

$$p = p^h + p' \,, \tag{19}$$

where $\left(\mathbf{u}^h, p^h\right)$ refer to the coarse scale and $(\mathbf{u}', p')$ represent the subscales. In this study we are using a residual-based approach (RBVMS) to determine the subscales, which are related to the residua as follows:

$$\mathbf{u}' = -\tau_M \mathbf{r}_M / \rho \,, \tag{20}$$

$$p' = -\rho \tau_C r_C \,, \tag{21}$$

here, $\mathbf{r}_M$ holds the residuum of the momentum equation, r_C denotes the residuum of the continuity equation, τ_M and τ_C are algebraic parameters inspired by stabilized finite element formulations. The residua $\mathbf{r}_M\left(\mathbf{u}^h, p^h\right)$ and $r_C\left(\mathbf{u}^h\right)$ are derived from (1) and (2) and can be stated as:

$$\mathbf{r}_M\left(\mathbf{u}^h, p^h\right) = \rho\left(\frac{\partial \mathbf{u}^h}{\partial t} + \mathbf{u}^h \cdot \nabla \mathbf{u}^h\right) - \nabla \cdot \boldsymbol{\sigma} - \mathbf{f} \,, \tag{22}$$

$$r_C\left(\mathbf{u^h}\right) = -\nabla \cdot \mathbf{u}^h \,. \tag{23}$$

For further details on the VMS formulation refer to Lins et al. (2010).

2.6 Finite element formulation

A space-discrete finite element formulation is used to approximate the problem. Let the standard trial and weight function spaces for the velocity and pressure be defined as $\mathbf{S}^h_{\mathbf{u}}$, $\mathbf{V}^h_{\mathbf{u}}$, $\mathbf{S}^h_p$ and $\mathbf{V}^h_p = \mathbf{S}^h_p$. So that the weak formulation of the Navier-Stokes equations including the residual-based variational multiscale method can be written as: Find $\mathbf{u}^h \in \mathbf{S}^h_{\mathbf{u}}$ and $p^h \in \mathbf{V}^h_{\mathbf{p}}$ such that $\forall \mathbf{w^h} \in \mathbf{V}^h_{\mathbf{u}}$ and $\forall q^h \in \mathbf{V}^h_p$ we have

$$\begin{aligned}
&\left(\rho\frac{\partial \mathbf{u}^h}{\partial t}, \mathbf{w}^h\right)_\Omega + \left(\left(\rho\mathbf{u}^h - \tau_M\mathbf{r}_M\right)\cdot\nabla\mathbf{u}^h, \mathbf{w}^h\right)_\Omega \\
&+ \left(\boldsymbol{\sigma}\left(p,\mathbf{u}\right), \varepsilon\left(\mathbf{w}^h\right)\right)_\Omega + \left(\nabla\cdot\mathbf{u}^h, q^h\right)_\Omega \\
&+ \left(\tau_M\mathbf{r}_M/\rho, \left(\rho\mathbf{u}^h - \tau_M\mathbf{r}_M\right)\cdot\nabla\mathbf{w}^h + \nabla q^h\right)_\Omega \\
&+ \left(\tau_C\rho\nabla\cdot\mathbf{u}^h, \nabla\cdot\mathbf{w}^h\right)_\Omega \\
&= \left(\mathbf{f}, \mathbf{w}^h\right)_\Gamma + \left(\mathbf{h}, \mathbf{w}^h\right)_{\Gamma_2} \,.
\end{aligned} \tag{24}$$

The parameters τ_M and τ_C are calculated by Akkerman et al. (2008):

$$\tau_M = \left(\frac{4}{\Delta t^2} + \mathbf{u}^h\cdot\mathbf{G}\mathbf{u}^h + C_1\nu^2\mathbf{G}\colon\mathbf{G}\right)^{-1/2} \,, \tag{25}$$

$$\tau_C = \left(\mathbf{g}\cdot\tau_M\mathbf{g}\right)^{-1} \,, \tag{26}$$

where $\mathbf{G}$ is a second rank metric tensor:

$$\mathbf{G} = \frac{\partial \boldsymbol{\xi}^T}{\partial \mathbf{x}} \frac{\partial \boldsymbol{\xi}}{\partial \mathbf{x}}, \tag{27}$$

here, g forms a vector of the column sums of $\frac{\partial \boldsymbol{\xi}}{\partial \mathbf{x}}$, so that:

$$\mathbf{g} = \{g_i\}, \tag{28}$$

$$g_i = \sum_{j=1}^{d} \left(\frac{\partial \boldsymbol{\xi}}{\partial x} \right)_{ji}. \tag{29}$$

The weak form of the VOF marking function (Eq. (13)) can be written as: Find $\phi \in Q$, so that, $\forall \Phi \in Z$

$$\left(\Phi, \frac{\partial \phi}{\partial t} \right)_{\Omega} + (\Phi, \mathbf{u} \cdot \nabla \phi)_{\Omega} + (\Phi, \phi \nabla \cdot \mathbf{u})_{\Omega} = 0, \tag{30}$$

where Q and Z are respectively the standard scalar weight and trial spaces. Adding SUPG stabilization terms to Eq. (30) leads to the following:

$$\begin{aligned} &\left(\Phi^h, \frac{\partial \phi^h}{\partial t} \right)_{\Omega} + \left(\Phi^h, \mathbf{u} \cdot \nabla \phi^h \right)_{\Omega} + \left(\Phi^h, \phi^h \nabla \cdot \mathbf{u} \right)_{\Omega} \\ &+ \left(\tau_M \mathbf{u} \cdot \nabla \Phi^h, \frac{\partial \phi^h}{\partial t} + \mathbf{u} \cdot \nabla \phi^h + \phi^h \nabla \cdot \mathbf{u} \right)_{\Omega_e} \\ &= 0. \end{aligned} \tag{31}$$

If needed, we can add to Eq. (31) a discontinuity capturing operator as in Bazilevs et al. (2007) and Catabriga et al. (2009), respectively for scalar and systems of advective-dominated equations.

2.7 Adaptive mesh refinement

All implementations are done using `libMesh`, an open-source software library for parallel adaptive finite element applications (Kirk et al., 2006). It supports parallel mesh refinement and coarsening. `libMesh` also interfaces with several external solver packages, such as PETSc (Balay et al., 2016) and Trilinos (Heroux et al., 2005). In particular, PETSc includes a large suite of parallel linear and nonlinear equation solvers. Despite providing several tools for mesh-based solvers, applications built upon `libMesh` need to reimplement many common finite element kernels, including assembly loops and time integration schemes. These kernels are typically related to the physics of the problem of interest and the numerical formulation adopted.

A local error estimator is used considering the error of an element relative to its neighbor elements in the mesh to drive the AMR procedure. As it is standard in `libMesh`, Kelly's error indicator is employed, which uses the $H1$-seminorm to estimate the error (Ainsworth & Oden, 2000). Apart from the element interior residual, the flux jumps across the inter-element faces have an influence on the element error. The flux jump of each face is computed and added to the error contribution of the cell. For both, the residual and flux jump, the value of the desired variables at each node is necessary. This is straightforward for nodal variables, e.g., velocity, pressure, VOF marker. However, for variables associated with each element, like the viscosity, the procedure gets more complicated. The element viscosity needs to be transformed into a nodal value. Thus, we use an $L2$-projection to obtain the nodal viscosities. Here, the matrix emanating from the $L2$-projection is diagonalized in the standard manner. In the case that more then one variable is used for the error estimation, the element errors of each variable are summed up. So that the error $\|e\|^2$ can be stated as:

$$\|e\|^2 = \sum_{i=1}^{n} \|e\|^2{}_i \,, \tag{32}$$

where $\|e\|^2{}_i$ is the error for each variable. In this study we use the VOF marker and the viscosity as variables for the error estimator, so that:

$$\|e\|^2 = \frac{\|e\|^2{}_\phi}{\max \|\mathbf{e}\|^2{}_\phi} + \frac{\|e\|^2{}_\eta}{\max \|\mathbf{e}\|^2{}_\eta} \,. \tag{33}$$

After computing all error values the elements are "flagged" for refining and coarsening regarding their relative error. This is done by a statistical element flagging strategy. It is assumed that the element error $\|e\|$ is distributed approximately in a normal probability function. Here, the statistical mean μ_s and standard deviation σ_s of all errors are calculated. Whether an element is flagged is depending on a refining (r_f) and a coarsening (c_f) fraction. For all errors $\|e\| < \mu_s - \sigma c_f$ the elements are flagged for coarsening and for all $\|e\| > \mu_s + \sigma r_f$ the elements are marked for refinement. The refinement is performed by local isotropic subdivision (h-refinement) with hanging nodes. Here, the refinement level is limited by a maximum h-level (h_{max}). The coarsening is done by h-restitution of subelements. (Peterson, 2008; Rossa & Coutinho, 2013; Kelly et al., 1983) In this study we use $h_{max} = 3$, a coarsening fraction $c_f = 0.001$ and a refining fraction $r_f = 0.995$.

3 RESULTS

In the following, we observe the effects of three continuous input factors: the maximum viscosity of the heavy fluid (η_{max}), the viscosity of the light fluid (η_L) and the density of the light fluid (ρ_L). Therefore, we perform a design of experiments (DOE) of 20 experiments of a collapsing column, also called dam break. The benchmark experiment simulates a collapsing non-Newtonian fluid using the $\mu(I)$-rheology (heavy fluid) surrounded by a light Newtonian fluid. Hereby, two different geometries are analyzed (included as a categorical input factor).

3.1 Experimental setup

The numerical experimental setup is equal to the simulations of Lagrée et al. (2011). The final time of the computations is 0.6 s with a fixed time step of $\Delta t = 0.0005$. The results are shown for a normalized time $t_n = t/\sqrt{H_0/g}$. Figure 1 sketches the geometry, the boundary conditions and the mesh of geometry 1 at the normalized time $t_n = 4.0$. The measures of the experiment are $l_x = 0.5$, $l_y = 0.21$, $H_0 = 0.1$ and $L_0 = 0.2$, so that the aspect ratio is $H_0/L_0 = 0.5$. The VOF marker of the fluid using the $\mu(I)$-rheology is $\phi = 1$ and of the light

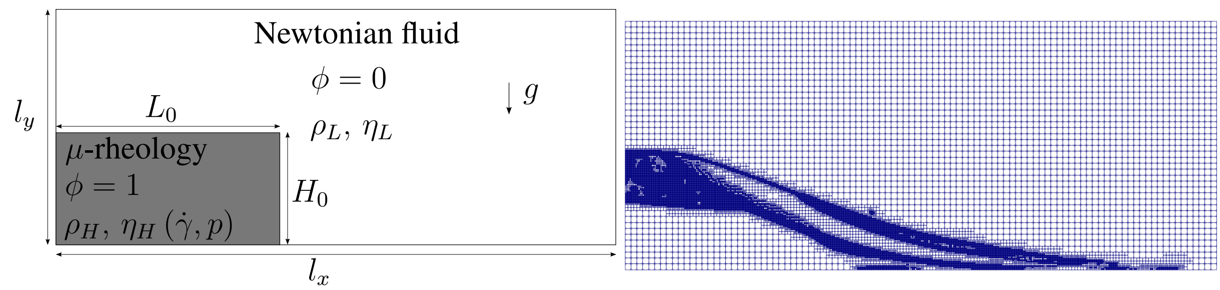

Figure 1: Geometry of the dam break with an aspect ratio of $H_0/L_0 = 0.5$ and mesh at normalized time $t_n = 4.0$.

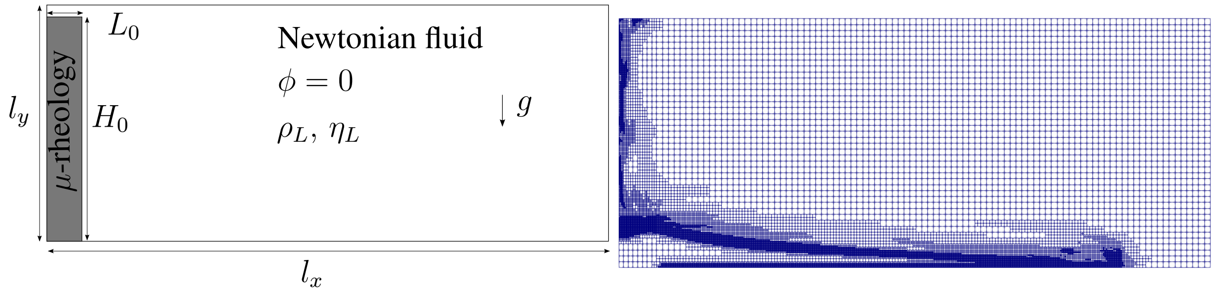

Figure 2: Geometry of the dam break with an aspect ratio of $H_0/L_0 = 6.26$ and mesh at normalized time $t_n = 4.0$.

fluid $\phi = 0$. Figure 2 illustrates geometry 2 and its mesh at $t_n = 4.0$. Here, the height and length of the heavy fluid are $H_0 = 0.2$ and $L_0 = 0.03195$, thus the aspect ratio is $H_0/L_0 = 6.26$.

The parameters of the $\mu(I)$-rheology are $\mu_s = 0.32$, $\mu_2 = 0.60$, $d = 5.3 \times 10^{-4}$, $\rho_g = 2500$, $I_0 = 0.4$ and $\eta_{min} = 0.1$. The maximum viscosity η_{max} varies between 200-2000. The light fluid holds a density and a Newtonian viscosity which varies between $\rho_L = 0.052$-25.0 and $\eta_L = 0.0001 - 0.01$. We assume the gravity to be $g = 9.81$. On the left and right wall we apply a slip boundary condition. On the top wall the velocity is free, the pressure and VOF marker are set to zero. On the bottom a no-slip boundary condition is added. Here, all computations are parallel, using 4 cores. The initial mesh is structured and has 100 bilinear quadrilateral elements in x direction and 42 elements in y-direction. Before the first time step the mesh is uniformly refined by two levels resulting in a mesh of $67,200$ elements. The linear systems are solved in parallel by Block-Jacobi + GMRES(50) with local ILU(1) preconditioning for both flow and transport solvers. The nonlinear solver is the inexact Newton-Krylov scheme. The initial GMRES tolerance is set to 10^6 and the minimum to 10^{10}. Nonlinear iterations are halted when the relative residual drops three orders of magnitude. The maximum number of linear iterations is 600 and the maximum number of nonlinear iterations is 10. The maximum number of linear iterations is 600 and the maximum number of nonlinear iterations is 10.

3.2 Design of experiments

In DOE, key input variable factors, which can be controlled in planned statistical patterns, are modified. The output, called response, is observed and related to the input variables. The Response Surface method (RSM) gives a prediction of input-output relations and thus, can be used to tune and optimize the experiment. The RSM calculates regression coefficients. A common regression model, also applied in this study, is the full quadratic polynomial model.

It contains linear and quadratic terms of each key input variable and their interaction terms. Creating a full DOE often needs a large number of experiments. To save time we run an optimal design. Here, just part of the experiments are realized. For our design we use D-optimality which maximizes the determinant of the information matrix of the design. Hereby, the variance is minimized and a computer algorithm chooses an optimal set of experiments from the full plan.

The model considers all second order terms. However, effects might mix with higher order effects and each other. The significant effects have a 95 % chance to be accurate. A full design plan would enhances this probability. The model generated by this method still gives a good impression of effects and is not as time consuming especially since several input variables are evaluated. This way, instead of 40 experiments we run only 20 experiments. For more information about the statistics background refer to Allen (2010). The DOE and RSM are executed with help of the software Minitab. [1]

3.3 Analysis of the results

Before starting the statistical experiments, results are compared and verified with the simulations of Lagrée et al. (2011). Figure 3 shows the column collapse for $t_n = 0.0,\ 1.0,\ 2.0,\ 3.0,\ 4.0.$ Since the visual results of the collapsing column are similar only experiment 14 and 18 are presented. Our computations match reasonable well the simulation results of Lagrée et al. (2011) (red dashed line). However, in their article Lagrée et al. (2011) do not state a specific density value of the heavy fluid used, but are mentioning that densities vary from below 2000 to 2500.

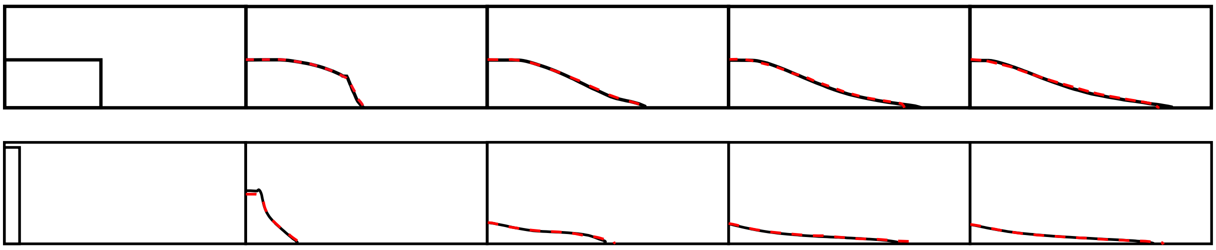

Figure 3: Results of the collapsing column of geometry 1 (up) and geometry 2 (down) for $t_n = 0.0,\ 1.0,\ 2.0,\ 3.0,\ 4.0$ **compared to simulations of Lagrée et al. (2011) (dashed line).**

In the first step the continuous key input variable factors are defined as the maximum viscosity of the heavy fluid (η_{max}), the viscosity of the light fluid (η_L) and the density of the light fluid (ρ_L). The geometry enters as a categorical factor. With help of DOE a statistical plan with D-optimality of the experiments is developed, which consists of 20 experiments. As output responses the mass loss, energy loss, flow front position, height position, CPU time, total number of linear iterations of the flow and transport solvers are observed. Considering the heavy fluid, mass conservation and a constant total energy is expected. Therefore, the loss of mass and energy over time is a good indicator of a working algorithm. Hereby, the mass m_{ts} and total energy e_{ts} of the heavy fluid are calculated and normalized for each time step. Afterwards, the magnitude of the difference to the initial mass m_0 and energy e_0 is summed up and divided by the total number of time steps n_{ts}. This gives a final value of the mass and energy variation for

[1]By Minitab Inc., State College, Pennsylvania, USA

each experiment:

$$\text{mass loss} = \left(\sum \sqrt{(1.0 - m_{ts}/m_0)^2} \right) / n_{ts} \,, \tag{34}$$

$$\text{energy loss} = \left(\sum \sqrt{(1.0 - e_{ts}/e_0)^2} \right) / n_{ts} \,. \tag{35}$$

A detailed plan of variables used in the simulations and the responses which are used to create the charts and plots can be found in Tab. 1 in the appendix. To begin the statistical analysis we provide Pareto charts regarding the responses. They consist of a bar diagram which indicates the standardized effects of the factors and their interaction on a chosen response. Each chart has a dashed line which indicates whether an effect is significant. For the analysis a significance level of $\alpha = 0.05$ is chosen. The Pareto chart displays absolute values of the effects. Thus, it points out influences of a variable, but not how it increases or decreases the response. This helps to rank and visualize the priority of effects on responses for a further analysis.

Figure 4 shows a Pareto chart of the standardized effects of the variables and their interactions on the CPU time. The horizontal bars illustrate the standardized effects, where the labels on the y-axis indicate the factors. C is for example the linear effect of the maximum viscosity, CC covers the quadratic term of the maximum viscosity and BC is the effect of the interaction of the density and the maximum viscosity. If the bars are crossing the red dashed line they are significant. The biggest influence has the linear and quadratic term of the maximum viscosity, as well as, the correlation of this parameter with the others. The geometry has also a significant effect on the CPU time. The quadratic factor of the viscosity of the light fluid has also an effect, whereas the effect of its linear term has no significance. The density of the light fluid has no significant influence.

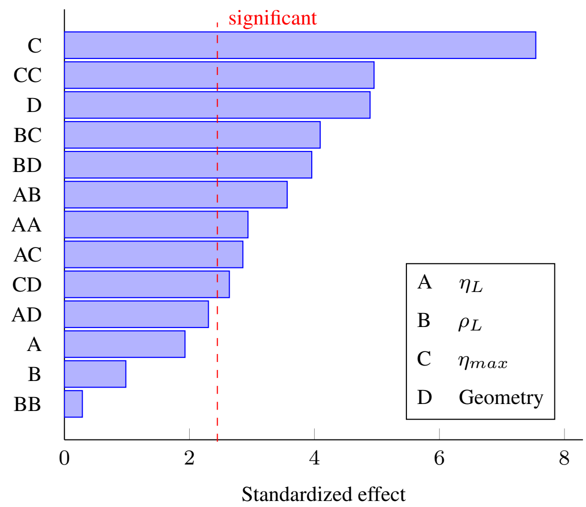

Figure 4: Pareto chart of the standardized effects of the variables and their interactions on the CPU time.

In Fig. 5a the standardized effects of the variables and their interactions on the total number of linear iterations of the flow solver are illustrated. The only significant effects are the interactions of the maximum viscosity with the geometry and with the density of the light fluid. The pure linear effect of the maximum viscosity is not significant. Figure 5b points out the influence of the variables and their interaction on the total number of linear iterations of the transport solver. It can be seen that the linear and quadratic terms of the maximum viscosity, the geometry and the viscosity of the light fluid have significant effects. The density has no significant influence at all.

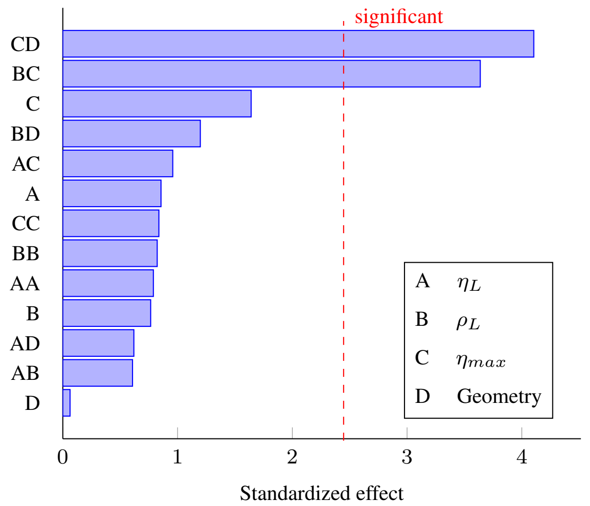

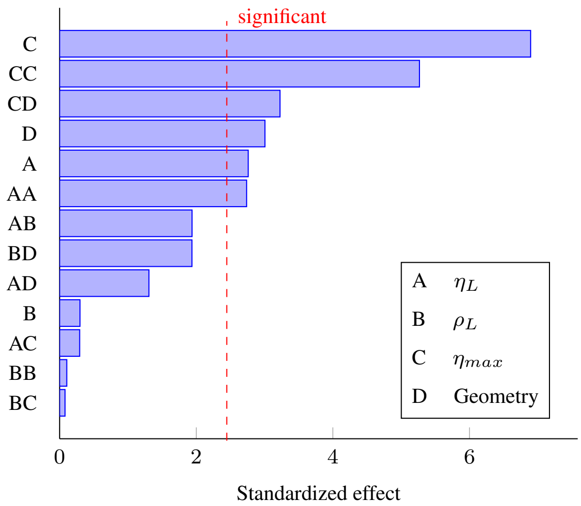

(a) Total number of linear iterations of the flow solver. (b) Total number of linear iterations of the transport solver.

Figure 5: Pareto chart of the standardized effects of the variables and their interactions.

In Figs. 6a and 6b the standardized effects of the variables and their interactions on the mass loss and the energy loss are shown. The Pareto charts show that none of the variables or their interactions have a significant influence on the mass or energy loss.

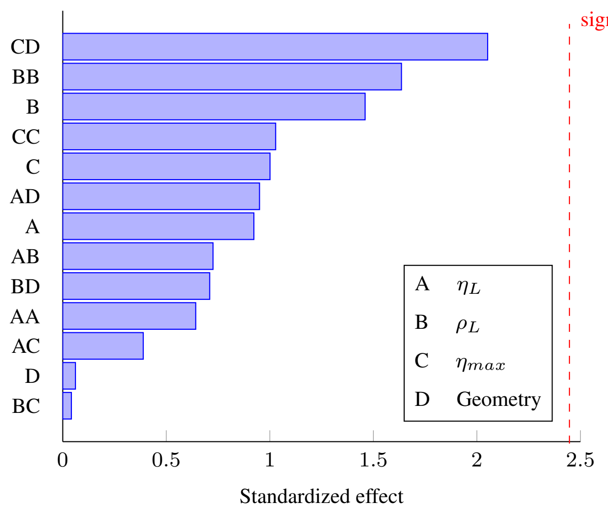

(a) Mass loss.

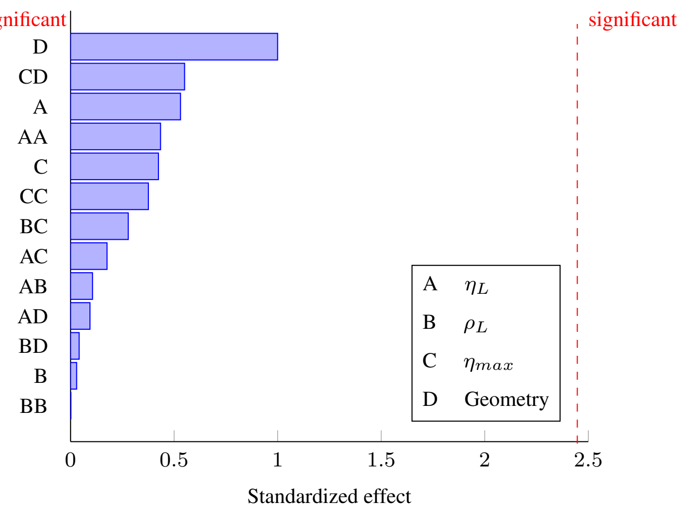

(b) Energy loss.

Figure 6: Pareto chart of the standardized effects of the variables and their interactions.

Figures 7a and 7b show the Pareto charts of the normalized height (H/H_0) and the flow front (L/L_0) positions at the time $t_n = 4.0$. The standardized effects of the variables and their interactions on the height are not significant. Whereas, the position of the flow front is strongly depending on the geometry, as well as, the interaction of the geometry with the density of the light fluid.

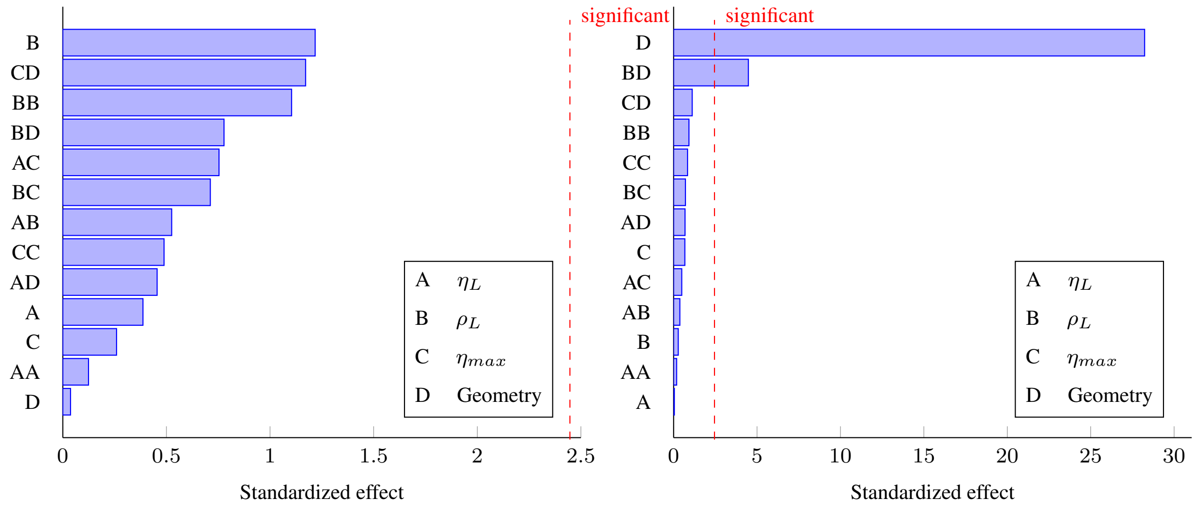

(a) Height position. **(b) Flow front position.**

Figure 7: Pareto chart of the standardized effects of the variables and their interactions.

For each response a full quadratic polynomial regression model is established. 3D surface plots, resulting from the RSM, illustrate the potential relationship between the three input factors and output responses. Hereby, the x and y-scales are the input variables and the z-scale shows the response. Meanwhile, the third continuous variable and the categorical variable (geometry) stay fixed. In Fig. 8 three surface plots are illustrated. They point out the relationships of the maximum viscosity, density and viscosity of the light fluid considering the response of the CPU time of geometry 1. It can be seen that the influence is mostly nonlinear, only the density has a quasi-linear effect. The density has no influence on the CPU time for the low values of the maximum viscosity, but for high values of the maximum viscosity the CPU time rises linearly with a higher density. Varying the viscosity of the light fluid a higher density leads to a higher CPU time. The viscosity of the light fluid always has a nonlinear effect on the CPU time. Here, lower and higher viscosities of the light fluid result in smaller CPU time than the medium values of viscosity. The maximum viscosity of the $\mu(I)$-rheology has a contrary effect, for high and low values the CPU time rises.

Figure 9 contains surface plots which illustrate the relationships of the maximum viscosity, density and viscosity of the light fluid considering the response of the CPU time of geometry 2. The surface plots resemble Fig. 8, but have some slight differences. In general, the CPU times of geometry 2 are shorter than of geometry 1. This can be related to the smaller area covered by the non-Newtonian fluid. Decreasing the viscosity of the light fluid for the low density values increases the CPU time. Besides that the effects are mostly the same, even though not as explicit, as for geometry 1.

Considering the 3D surface plots combined with the Pareto chart of Fig. 4, it confirms that the maximum viscosity and geometry have the biggest effect on the CPU time. Their influence is consistent in all plots. The density and viscosity of the light fluid have no significant effects. The effects of the density and viscosity are different, even contradictory, for the two geometries or have no influence.

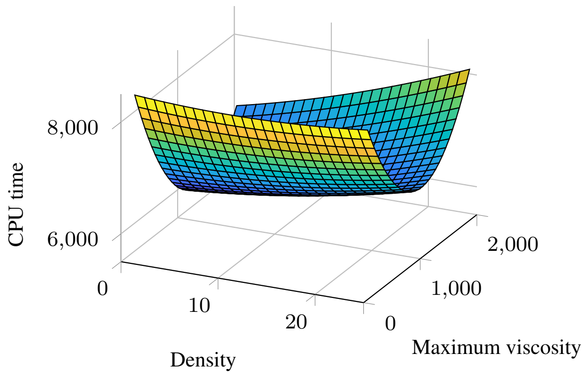

(a) Relationship between η_{max} and ρ_L, $\eta_L = 0.001$.

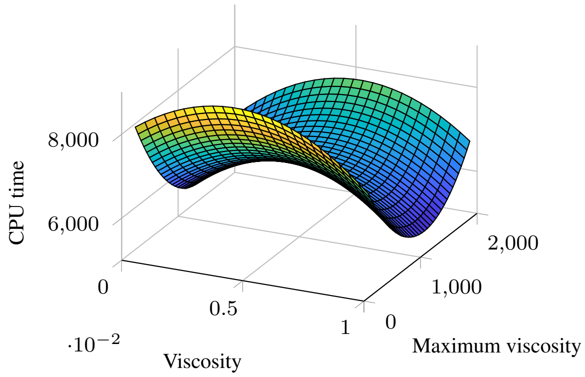

(b) Relationship between η_{max} and η_L, $\rho_L = 2.5$.

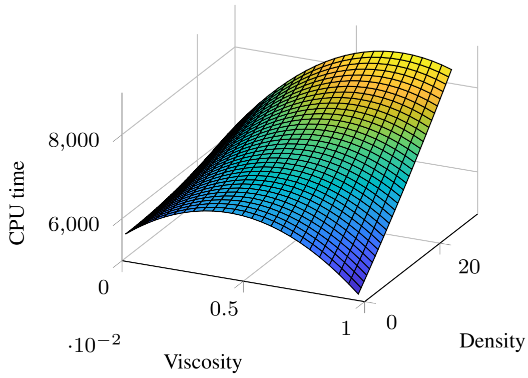

(c) Relationship between ρ_L and η_L, $\eta_{max} = 1050$.

Figure 8: 3D surface plots of the CPU time for geometry 1.

Figure 10 shows the 3D surface plots of the relationships between the variables responding the normalized flow front position at $t_n = 4.0$ of geometry 1. It can be seen that the effects of the variables are nonlinear. The influence of the viscosity of the light fluid is minor since the flow front position almost stays constant varying the viscosity, whereas the density of the light fluid has a clear effect. For lower and higher densities the flow front is behind. The maximum viscosity of the non-Newtonian fluid leads for the high and low values to an advanced flow front position.

In Fig. 11 the 3D surface plots of the relationships of the variables on the normalized flow front position at $t_n = 4.0$ of geometry 2 can be seen. The plots are very different from the plots of geometry 1. First of all, the absolute value of the flow front position is much more advanced compared to geometry 1, which is related to the height of the columns. But also the plot shape itself differs a lot from the plots in Fig. 10. A high maximum viscosity of the $\mu(I)$-rheology leads to a more advanced flow front position. Whereas, a high value of the density and of the viscosity of the light fluid keep the flow front position at lower values. Even though the effects are nonlinear, the quadratic characteristic is not as distinct as for geometry 1.

Comparing those results with the Pareto chart in Fig. 7b, we can see that only the geometry has a significant influence on the response of the flow front position and indeed the absolute values between the geometries vary a lot. Even though the Pareto chart does not show an overall significant influence of the maximum viscosity, density and viscosity of the light fluid, they have effects within the experiments of each geometry. However, the changes are little

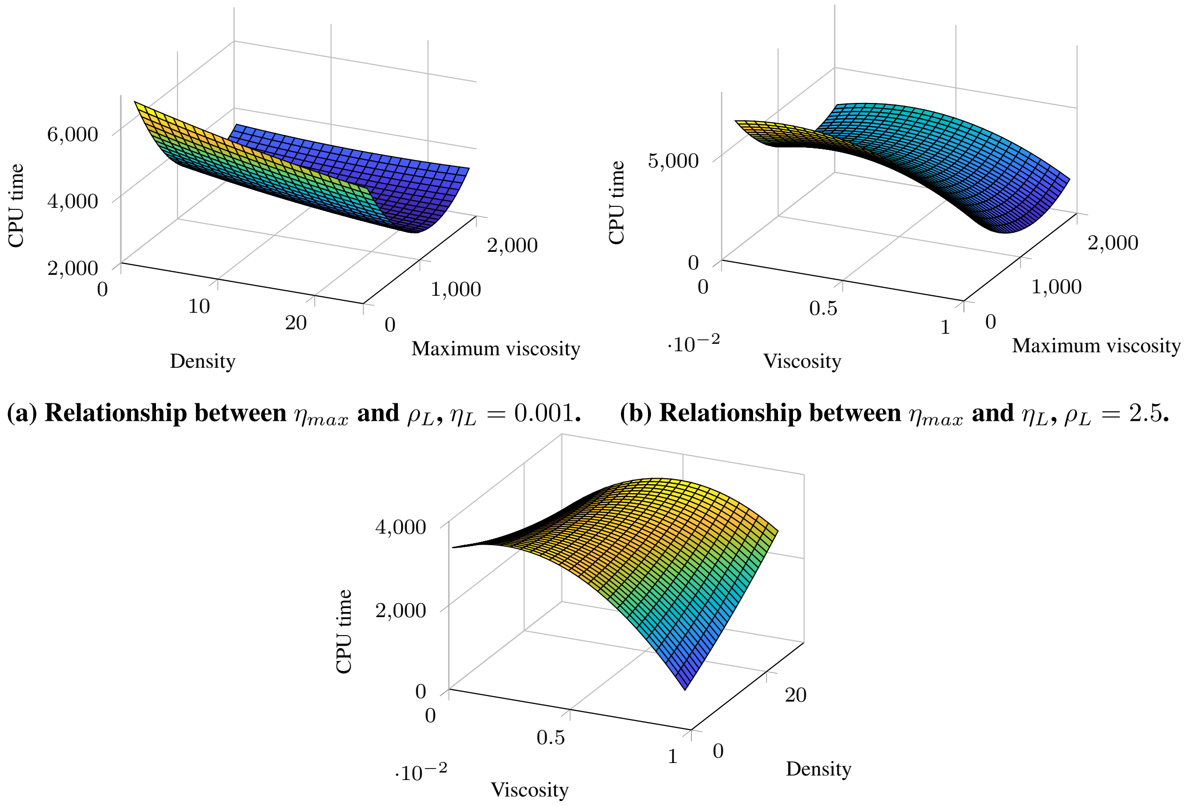

(a) Relationship between η_{max} and ρ_L, $\eta_L = 0.001$.

(b) Relationship between η_{max} and η_L, $\rho_L = 2.5$.

(c) Relationship between ρ_L and η_L, $\eta_{max} = 1050$.

Figure 9: 3D surface plots of the CPU time of geometry 2.

compared to the influence of the geometry. Moreover, the tendency is also different for the two geometries.

During the experiments some simulations, especially of geometry 2, showed difficulties. At a certain point the light fluid enters under the heavy fluid due to instabilities. Therefore, the fluid advances faster since it is slipping over the light fluid. This instability is based on the constellation of the variables together with the experiment setup. To avoid this the range of variables needs to be changed and the regularization needs to be adapted. However, it is also a point of this study to show that with some constellations we find those problems.

4 CONCLUSION

A column collapse is simulated applying the $\mu(I)$-rheology using VMS, AMR and regularization strategies. DOE and RSM are helpful tools to analyze the effects and relationships of the input variable factors. Effects and relationships of the maximum viscosity of the $\mu(I)$-rheology and the density and viscosity of the light surrounding fluid on output responses are evaluated by 20 experiments building regression models. The effects of the variables and their interactions are examined by statistical analysis, including Pareto charts and 3D surface plots. The influences are nonlinear and complex. A too high or low maximum viscosity augments the computing time. A low fluid density combined with a high viscosity of the light fluid reduces the CPU time. The flow front position differs a lot for the two geometries. The flow front position of geometry 1 is more advanced for a low or high maximum viscosity and the medium

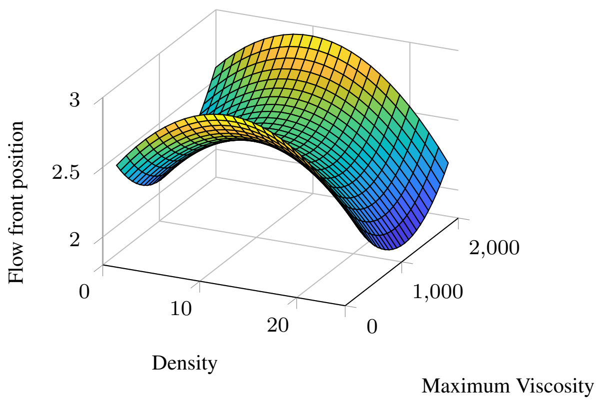

(a) **Relationship between η_{max} and ρ_L, $\eta_L = 0.001$.**

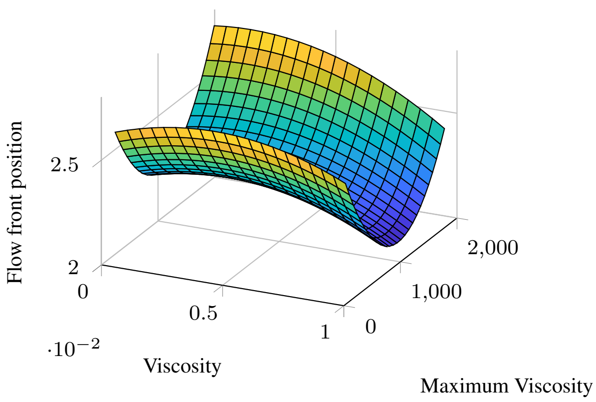

(b) **Relationship between η_{max} and η_L, $\rho_L = 2.5$.**

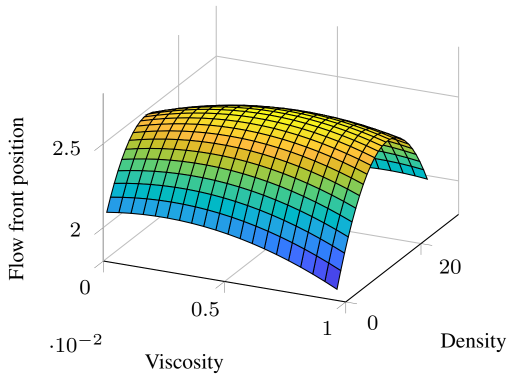

(c) **Relationship between ρ_L and η_L, $\eta_{max} = 1050$.**

Figure 10: 3D surface plots of the flow front position time of geometry 1.

values of the density of the light fluid. For a high viscosity, the solver has more difficulties to converge and therefore, the flow front proceeds more. A too low maximum viscosity allows the fluid to flow more and thus, has a more advanced flow front position. The viscosity of the light fluid has no major effect on the flow front position of geometry 1.

The flow front position of geometry 2 is advanced for low density and viscosity values of the light fluid and a high maximum viscosity of the $\mu(I)$-rheology. This happens due to solver convergence problems as the light fluid enters under the heavy fluid causing a slip boundary condition. Consequently, those constellations of variables should be avoided. The maximum viscosity to limit the $\mu(I)$-rheology should be chosen in an intermediate value interval. Here, also less computation time is needed. Too low density and viscosity values of the light fluid, even though it might represent the physics of air better, lead to convergence problems. The density of the light fluid has a major influence on the flow front position since it adds to a higher hydrostatic pressure, which results in less flowing of the non-Newtonian fluid. This effect can be avoided by applying the boundary condition for zero pressure on the top of the heavy fluid. However, this is far more complicated since the interface is moving every time step. The effect of small densities of the light fluid on the pressure is negligible.

It needs to be mentioned that we analyze only 20 experiments. According to D-optimality, evaluating three continuous factors and one categorical factor, those are part of a full statistical plan which involves 40 experiments. Even though it is possible to conclude trends and effects, a full statistical plan would provide clearer and more founded results. However, these 40 experi-

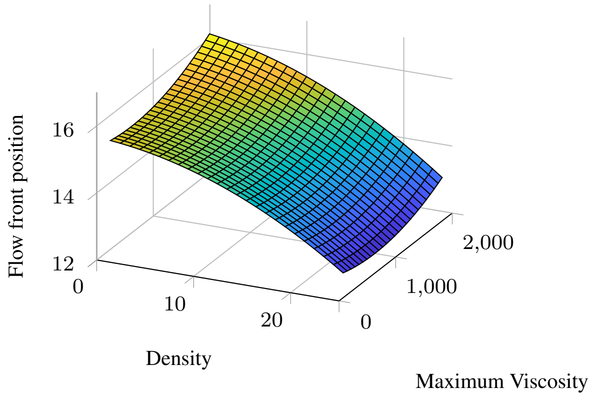

(a) Relationship between η_{max} and ρ_L, $\eta_L = 0.001$.

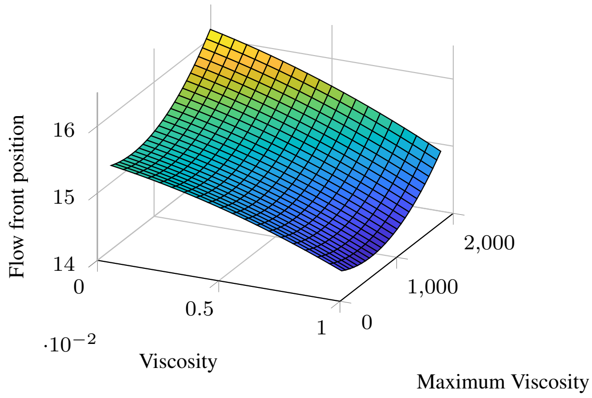

(b) Relationship between η_{max} and η_L, $\rho_L = 2.5$.

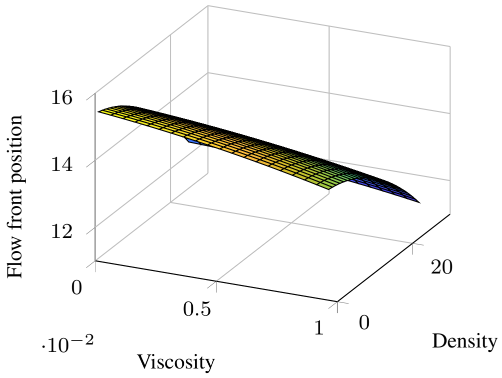

(c) Relationship between ρ_L and η_L, $\eta_{max} = 1050$.

Figure 11: 3D surface plots of the flow front position time of geometry 2.

ments were too time intensive for this study. In general, statistical analysis is also a useful tool to verify a model and its plausibility. Moreover, 3D surface plots of the relationships are achieved by a full quadratic polynomial regression models. Better results might be accomplished also by fitting the data to a different function type.

All in all, the present study shows the difficulties and complexity of computing non-Newtonian two phase flow using the $\mu(I)$-rheology. Even though some statements could be made, the conditions may vary for different test cases.

ACKNOWLEDGEMENTS

The research has received funding from the European Union's Horizon 2020 Programme (2014-2020) under the HPC4E Project (www.hpc4e.eu), grant agreement n 689772, and from the Brazilian Ministry of Science, Technology, Innovation and Communications through Rede Nacional de Pesquisas (RNP). This work is also partially supported by CNPq, FAPERJ, Capes and Petrobras. Furthermore, we would like to thank Prof. Bernhard Gesenhues from the University of Applied Science Darmstadt for his invaluable help and advice on DOE.

APPENDIX

The intermediate values of the maximum viscosity of the heavy fluid (η_{max}), the viscosity of the light fluid (η_L) and the density of the light fluid (ρ_L) are chosen regarding the experiments of Lagrée et al. (2011). In a next step values are alternated according to DOE.

Table 1: Experiment data and results

Exp.	η_L	ρ_L	η_{max}	Geo.	Mass loss	Energy loss	Height	Flow front	CPU time	Flow LI	Transport LI
1	0.001	2.5	1500	2	0.0064	0.01	0.20	15.60	2919.23	266916	6140
2	0.001	25	1050	2	0.0020	0.012	0.20	12.15	2611.61	365360	6402
3	0.001	0.052	1050	2	0.0031	0.027	0.20	15.64	3339.60	233629	6174
4	0.001	2.5	50	2	0.0049	0.021	0.17	15.64	7281.94	173582	5236
5	0.0005	2.5	1050	2	0.0041	0.027	0.18	15.64	3748.98	242553	6476
6	0.0001	0.25	2000	1	0.0006	0.011	0.98	2.50	6290.90	596030	6070
7	0.01	10	1500	1	0.0005	0.0092	0.98	2.23	6447.70	615077	6133
8	0.0001	0.25	200	1	0.0023	0.0022	0.89	2.38	7954.34	297424	5270
9	0.0001	25	200	1	0.0023	0.0022	0.89	2.38	7956.84	297424	5270
10	0.005	2.5	1050	2	0.0068	0.0056	0.20	14.58	3179.12	273715	6070
11	0.01	0.25	200	1	0.0014	0.0032	0.89	2.32	6931.35	278634	5347
12	0.005	2.5	1050	1	0.0023	0.0039	0.97	2.34	6821.73	543733	5931
13	0.01	0.25	2000	1	0.0009	0.011	0.98	2.32	6238.88	598313	6121
14	0.0001	25	2000	1	0.0009	0.012	0.98	2.09	7464.43	905136	6077
15	0.0001	25	200	1	0.0023	0.0042	0.89	2.11	7705.75	369490	5254
16	0.001	2.5	1050	2	0.0077	0.0069	0.20	15.59	3334.55	275121	6101
17	0.0005	0.25	1500	2	0.0052	0.0081	0.20	15.60	3021.8	268737	6111
18	0.01	25	200	2	0.0016	0.0087	0.20	11.86	4843.66	262427	5650
19	0.0001	0.25	200	2	0.0032	0.0023	1.52	14.87	6375.77	261167	5564
20	0.01	25	1500	2	0.0037	0.017	0.21	11.94	3017.31	339661	6262

REFERENCES

Ahmed, N., Chacón Rebollo, T., John, V., & Rubino, S., 2015. A Review of Variational Multiscale Methods for the Simulation of Turbulent Incompressible Flows. *Archives of Computational Methods in Engineering*, vol. 24, pp. 115.

Ainsworth, M., & Oden, J. T., 2000. *A Posteriori Error Estimation in Finite Element Analysis*. John Wiley & Sons, Inc.

Akkerman, I., Bazilevs, Y., Calo, V. M., Hughes, T. J. R., & Hulshoff, S., 2008. The role of continuity in residual-based variational multiscale modeling of turbulence. *Computational Mechanics*, vol. 41, no. 3, pp. 371.

Allen, T. T., 2010. *Introduction to Engineering Statistics and Lean Sigma*. Springer London, London.

Balay, S., Abhyankar, S., Adams, M., Brown, J., Brune, P., Buschelman, K., Dalcin, L., Eijkhout, V., Gropp, W., Karpeyev, D., Kaushik, D., Knepley, M., McInnes, L. C., Rupp, K., Smith, B., Zampini, S., Zhang, H., & Zhang, H., 2016. PETSc Users Manual. Tech. rep., Argonne National Laboratory.

Bazilevs, Y., Calo, V. M., Tezduyar, T. E., & Hughes, T. J. R., 2007. YZβ discontinuity capturing for advection-dominated processes with application to arterial drug delivery. *International Journal for Numerical Methods in Fluids*, vol. 54, pp. 593.

Bercovier, M., & Engelman, M., 1980. A finite-element method for incompressible non-Newtonian flows. *Journal of Computational Physics*, vol. 36, no. 3, pp. 313.

Castillo, E., & Codina, R., 2014a. Stabilized stress-velocity-pressure finite element formulations of the Navier-Stokes problem for fluids with non-linear viscosity. *Computer Methods in Applied Mechanics and Engineering*, vol. 279, pp. 554.

Castillo, E., & Codina, R., 2014b. Variational multi-scale stabilized formulations for the stationary three-field incompressible viscoelastic flow problem. *Computer Methods in Applied Mechanics and Engineering*, vol. 279, no. September, pp. 579.

Catabriga, L., de Souza, D. A. F., Coutinho, A. L. G. A., & Tezduyar, T. E., 2009. Three-dimensional edge-based SUPG computation of inviscid compressible flows with YZβ shock-capturing. *Journal of Applied Mechanics*, vol. 76, no. 2, p. 21208.

Chauchat, J., & Médale, M., 2014. A three-dimensional numerical model for dense granular flows based on the μ-rheology. *Journal of Computational Physics*, vol. 256, no. April, pp. 696.

Codina, R., & Castillo, E., 2016. Numerical analysis of a stabilized finite element approximation for the three- field linearized viscoelastic fluid problem using arbitrary interpolations. *ESAIM: Mathematical Modelling and Numerical Analysis*.

Elias, R. N., & Coutinho, A. L. G. A., 2007. Stabilized edge-based finite element simulation of free-surface flow. *International Journal for Numerical Methods in Fluids*, vol. 54, pp. 965.

Forterre, Y., & Pouliquen, O., 2008. Flows Of Dense Granular Media. *Annual Review Of Fluid Mechanics*, vol. 40, no. 1, pp. 1.

Frigaard, I. A., & Nouar, C., 2005. On the usage of viscosity regularisation methods for visco-plastic fluid flow computation. *Journal of Non-Newtonian Fluid Mechanics*, vol. 127, no. 1, pp. 1.

Gravemeier, V., 2003. *The Variational Multiscale Method for Laminar and Turbulent Incompressible Flow Volker Gravemeier*. Phd thesis, University Stuttgart.

Heroux, M. A., Phipps, E. T., Salinger, A. G., Thornquist, H. K., Tuminaro, R. S., Willenbring, J. M., Williams, A., Stanley, K. S., Bartlett, R. A., Howle, V. E., Hoekstra, R. J., Hu, J. J., Kolda, T. G., Lehoucq, R. B., Long, K. R., & Pawlowski, R. P., 2005. An overview of the Trilinos project. *ACM Transactions on Mathematical Software*, vol. 31, no. 3, pp. 397.

Hughes, T. J., Feijóo, G. R., Mazzei, L., & Quincy, J.-B., 1998. The variational multiscale methoda paradigm for computational mechanics. *Computer Methods in Applied Mechanics and Engineering*, vol. 166, no. 1-2, pp. 3.

Hughes, T. J. R., 1995. Multiscale phenomena: Green's functions, the Dirichlet-to-Neumann formulation, subgrid scale models, bubbles and the origins of stabilized methods. *Computer Methods in Applied Mechanics and Engineering*, vol. 127, no. 1-4, pp. 387.

Hughes, T. J. R., Scovazzi, G., & Franca, L. P., 2004. Multiscale and Stabilized Methods. *Encyclopedia of Computational Mechanics*, vol. 3:2.

Ionescu, I. R., Mangeney, A., Bouchut, F., & Roche, O., 2015. Viscoplastic modeling of granular column collapse with pressure-dependent rheology. *Journal of Non-Newtonian Fluid Mechanics*, vol. 219, pp. 1.

John, V., 2006. On large Eddy simulation and variational multiscale methods in the numerical simulation of turbulent incompressible flows. *Applications of Mathematics*, vol. 51, no. 4, pp. 321.

Jop, P., Forterre, Y., & Pouliquen, O., 2005. Crucial role of side walls for granular surface flows: consequences for the rheology. *Journal of Fluid Mechanics*, vol. 541, no. 2005, pp. 167.

Jop, P., Forterre, Y., & Pouliquen, O., 2006. A constitutive law for dense granular flows. *Nature*, vol. 441, no. 7094, pp. 727.

Kelly, D. W., Gago, J. P. D. S. R., Zienkiewicz, O. C., & Babuska, I., 1983. A posteriori error analysis and adaptive processes in the finite element method: Part I - Error analysis. *International Journal for Numerical Methods in Engineering*, vol. 19, no. June 1982, pp. 1593.

Kirk, B. S., Peterson, J. W., Stogner, R. H., & Carey, G. F., 2006. libMesh : a C++ library for parallel adaptive mesh refinement/coarsening simulations. *Engineering with Computers*, vol. 22, no. 3-4, pp. 237.

Lagrée, P.-Y., Staron, L., & Popinet, S., 2011. The granular column collapse as a continuum: validity of a two-dimensional NavierStokes model with a μ(I)-rheology. *Journal of Fluid Mechanics*, vol. 686, no. c, pp. 378.

Lins, E. F., Elias, R. N., Rochinha, F. A., & Coutinho, A. L. G. A., 2010. Residual-based variational multiscale simulation of free surface flows. *Computational Mechanics*, vol. 46, no. 4, pp. 545.

Masud, A., & Kwack, J., 2011. A stabilized mixed finite element method for the incompressible shear-rate dependent non-Newtonian fluids: Variational Multiscale framework and consistent linearization. *Computer Methods in Applied Mechanics and Engineering*, vol. 200, no. 5-8, pp. 577.

Mitsoulis, E., 2007. Flows of viscoplastic materials: Models and computations. *Rheology Reviews*, vol. 2007, pp. 135 .

Moreno, E., & Cervera, M., 2015. Elementos finitos mixtos estabilizados para flujos confinados de Bingham y de Herschel-Bulkley Parte II: soluciones numéricas. *Revista Internacional de Métodos Numéricos para Cálculo y Diseño en Ingeniería*, vol. 32, no. 3, pp. 131.

Moreno, E., Larese, A., & Cervera, M., 2016. Modelling of Bingham and Herschel-Bulkley flows with mixed P1/P1 finite elements stabilized with orthogonal subgrid scale. *Journal of Non-Newtonian Fluid Mechanics*, vol. 228, pp. 1.

Papanastasiou, T. C., 1987. Flows of Materials with Yield. *Journal of Rheology*, vol. 31, no. 5, p. 385.

Peterson, J. W., 2008. *Parallel Adaptive Finite Element Methods for Problems in Natural Convection*. Ph.D. thesis, The University of Texas at Austin.

Pouliquen, O., 1999. Scaling laws in granular flows down rough inclined planes. *Physics of Fluids*, vol. 11, no. 3, p. 542.

Pouliquen, O., & Forterre, Y., 2002. Friction law for dense granular flows: application to the motion of a mass down a rough inclined plane. *Journal of Fluid Mechanics*, vol. 453, no. 1998, p. 19.

Rasthofer, U., & Gravemeier, V., 2017. Recent Developments in Variational Multiscale Methods for Large-Eddy Simulation of Turbulent Flow. *Archives of Computational Methods in Engineering*.

Riber, S., Valette, R., Mesri, Y., & Hachem, E., 2016. Adaptive variational multiscale method for bingham flows. *Computers and Fluids*, vol. 138, pp. 51.

Roquet, N., Michel, R., & Saramito, P., 2000. Estimations d'erreur pour un fluide viscoplastique par éléments finis Pk et maillages adaptés. *Comptes Rendus de l'Académie des Sciences - Series I - Mathematics*, vol. 331, no. 7, pp. 563.

Roquet, N., & Saramito, P., 2003. An adaptive finite element method for Bingham fluid flows around a cylinder. *Computer Methods in Applied Mechanics and Engineering*, vol. 192, no. 31-32, pp. 3317.

Rossa, A. L., & Coutinho, A. L. G. A., 2013. Parallel adaptive simulation of gravity currents on the lock-exchange problem. *Computers and Fluids*, vol. 88, pp. 782.

Saramito, P., & Roquet, N., 2001. An adaptive finite element method for viscoplastic fluid flows in pipes. *Computer Methods in Applied Mechanics and Engineering*, vol. 190, no. 40-41, pp. 5391.

Staron, L., Lagrée, P.-Y., & Popinet, S., 2014. Continuum simulation of the discharge of the granular silo. *The European Physical Journal E*, vol. 37.

Staron, L., Lagrée, P.-Y., Ray, P., & Popinet, S., 2013. Scaling laws for the slumping of a Bingham plastic fluid. *Journal of Rheology*, vol. 57, no. 4, p. 1265.

Syrakos, A., Georgiou, G. C., & Alexandrou, A. N., 2013. Solution of the square lid-driven cavity flow of a Bingham plastic using the finite volume method. *Journal of Non-Newtonian Fluid Mechanics*, vol. 195, pp. 19.

Zhang, J., 2010. An augmented Lagrangian approach to Bingham fluid flows in a lid-driven square cavity with piecewise linear equal-order finite elements. *Computer Methods in Applied Mechanics and Engineering*, vol. 199, no. 45-48, pp. 3051.